Resonant scattering of surface acoustic waves by arrays of magnetic stripes ⊘

Y. Au ✉ iD ; O. S. Latcham iD ; A. V. Shytov iD ; V. V. Kruglyak iD

Check for updates

View Online   Export Citation   CrossMark

Resonant scattering of surface acoustic waves by arrays of magnetic stripes

View Online   Export Citation   CrossMark

Y. Au,[a] 🆔 O. S. Latcham, 🆔 A. V. Shytov, 🆔 and V. V. Kruglyak 🆔

AFFILIATIONS

Department of Physics and Astronomy, University of Exeter, Stocker Road, Exeter EX4 4QL, United Kingdom

[a]Author to whom correspondence should be addressed: y.au@exeter.ac.uk

ABSTRACT

Owing to magnetoelastic coupling, surface acoustic waves (SAWs) may be scattered resonantly by magnetic elements, such as nickel stripes. The scattering may be further enhanced via the Borrmann effect when the elements are organized into an array that matches the acoustic wavelength. We use finite-element modeling to consider single- and double-layer stripes patterned on top of a lithium niobate surface that carries Love surface waves. We do observe enhancement in the coupling for single-layer stripes, but only for Gilbert damping below its realistic value. For double-layered stripes, a weak yet clear and distinct signature of Bragg reflection is identified far away from the acoustic band edge, even for a realistic damping value. Double-layered stripes also offer better magnetic tunability when their magnetic period is different from the periodicity of elastic properties of the structure because of staggered magnetization patterns. The results pave the way for the design of magnetoacoustic metamaterials with an enhanced coupling between propagating SAWs and local magnetic resonances and for the development of reconfigurable SAW-based circuitry.

19 December 2023 14:32:54

I. INTRODUCTION

Surface acoustic waves (SAWs) have long been used for filtering in data communication[1] and as radio-frequency identification tags in security applications.[2] However, often overlooked is a more ambitious application of SAWs as a signal carrier in on-chip wave-based computation (a.k.a. phononics[3]) where SAWs could play a role similar to that of electromagnetic waves in photonics[4] and spin waves (SWs) in magnonics.[5] These wave-based paradigms are often seen as hopeful alternatives to replace traditional CMOS technologies in the quest to lower power consumption of computing devices. Among them, phononics and magnonics are of particular interest because of the reduced group and phase velocities of SAWs and SWs (as compared to the electromagnetic waves). The resulting time delay can be employed, e.g., in the burgeoning field of time-multiplexed reservoir computing.[6] The primary advantage of phononics over magnonics is the readiness of SAWs to be excited and detected electrically (through piezoelectric materials). However, the drawback of phononics lies in the lack of tunability and reconfigurability of SAW's propagation circuitry. This contrasts with SWs, for which propagation is tunable by the bias magnetic field and reconfigurable by switching the static magnetization background. It is,

therefore, attractive to combine phononics and magnonics (namely "magnetoacoustics"[7,8]) to retain the advantages of both SAWs and SWs.

Although the effect of magnetoelastic coupling on acoustic propagation was studied in Refs. 9–15 by measuring transmission through an acoustic material under a continuous magnetic film, the possibility of further patterning the film into periodic nanostructures to form SAW metamaterials has remain largely unexplored. Early attempts to probe simultaneously phononic and magnonic properties of periodic magnetic stripe arrays did not detect any hybridization of the acoustic wave and spin wave.[16,17] Later studies concentrated on a simplistic one-dimensional (1D) model in which an array of magnetic slabs was interleaved with a non-magnetic spacer that carries bulk acoustic waves. Such systems were predicted to be effective bulk acoustic wave-driven spin wave transducers.[18–20] On the other hand, Latcham et al.[21] suggested that magnetoelastic interaction can be enhanced in such a 1D metamaterial and have found that the coupling between magnetic modes of the nickel stripes and bulk acoustic waves at frequencies in and around acoustic bandgaps can lead to a magneto-acoustic version of the Borrmann effect and magnetically induced

transparency (see examples from the literatures[22]), but only under an unrealistic assumption of the low Gilbert damping factor value in nickel. It is, therefore, intriguing whether these phenomena could be observed for SAWs and under more realistic assumptions about magnetic damping. Importantly, excitation and detection of SAWs using lithographically made interdigital transducers (IDTs) is a standard technique. The use of SAWs is also desirable technologically because SAW metamaterials can be fabricated lithographically, which is easier compared to construction of bulk acoustic metamaterials.

Besides unrealistic damping strength, Ref. 21 considered an unrealistic one-dimensional geometry, with the acoustic wave propagated in the bulk. Practical phononic devices usually employ Rayleigh or Love waves propagating on a surface of a piezoelectric, such as lithium niobate. One may wonder if the findings of Ref. 21 hold in this setup, with magnetic elements attached to the surface of a piezoelectric. It is also interesting whether one can improve upon these findings by engineering the magnetic elements.[23] To this end, we perform finite-element modeling of such a structure, which is described in detail in Sec. II. We introduce the design of an array of nickel stripes fabricated on top of a $LiNbO_3$ substrate that exhibits the Bragg reflection and Borrmann effect for SAWs. The Borrmann effect occurs at frequencies near to bandgap edges,

where the propagating SAWs are slowed down and eventually form standing modes. This slowing and (at one of the two bandgap edges) concentration of the SAWs in the magnetic stripes can enhance coupling between the SAWs and the SW modes of the stripes [see Fig. 1(c)]. The enhancement is desirable as a way to mitigate inherent weakness of the magnetoelastic coupling. The same target attenuation figure, therefore, could be achieved for a shorter propagation length and smaller size of the device. The obvious drawback of the Borrmann effect is that the coupling is enhanced only near to the bandgap edges, where purely acoustic attenuation is already substantial. Also, the Bragg scattering of the SAWs is determined by the period of the structure and is not field-tunable. In Sec. III, we show how the issue can be circumvented in an appropriately designed array of double-layer nickel stripes. The double layer can be perceived as a prototype synthetic antiferromagnetic structure and provides a unique opportunity to switch off and on coupling between SAWs and local magnetic resonances by aligning the double layer's magnetizations into the parallel or anti-parallel state. Subsequently, it is possible to achieve purely magnetic Bragg scattering of SAWs with frequencies far away from the non-tunable acoustic bandgap. The results unlock the possibility for spatial periodic structure enhancement of the magneto-acoustic coupling that is free from an uncontrollable attenuation
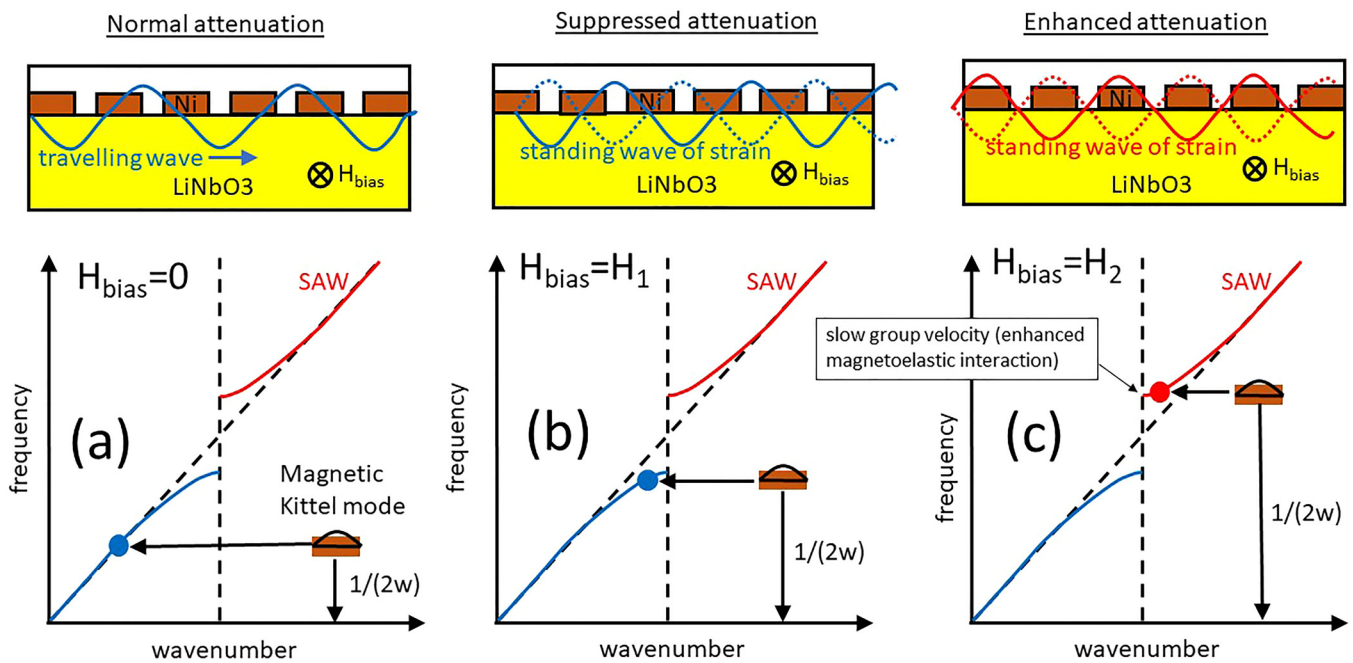
FIG. 1. Illustration of Borrman's effect in a magnetoacoustic system. (a) Nickel stripe (width equals w) with fixed spatial periodicity fabricated on top of a $LiNbO_3$ substrate leads to the formation of an acoustic bandgap in the dispersion curve of the SAW in the frequency–momentum space. When $H_{bias} = 0$, the magnetic Kittel mode in the stripe couples to SAW with frequency far below the bandgap. SAW travels through the nickel array structure unhindered. (b) H_{bias} is raised to H_1, which relocates the SAW-magnetic mode hybridization point to the lower edge of the acoustic bandgap. Standing wave of SAW forms in the nickel array with the maxima of the strain located in the gap between the nickel stripes. This leads to suppression of interaction between the SAW and magnetic resonance (suppressed magnetic attenuation of SAW). (c) H_{bias} is further increased to H_2, which relocates the hybridization point to the upper acoustic band edge. In this case, the standing wave strain maxima are located inside the nickel stripes themselves, leading to the enhancement of interaction between the SAW and the magnetic mode (enhanced magnetic attenuation of SAW).

background. The coupling control by magnetization switching provides reconfigurability; some potential applications of which are discussed in Sec. IV.

II. SINGLE-LAYER STRIPE ARRAY

Figure 2(a) describes the construction of the proposed metamaterial and its parameters used in our numerical model. We consider an array consisting of $N_{dev} = 20$ nickel stripe elements with infinite length and with cross section width w and thickness d. The array sits on the surface of a 41° YX LiNbO₃ substrate and is covered by an aluminum capping layer with thickness d_{cap}. The
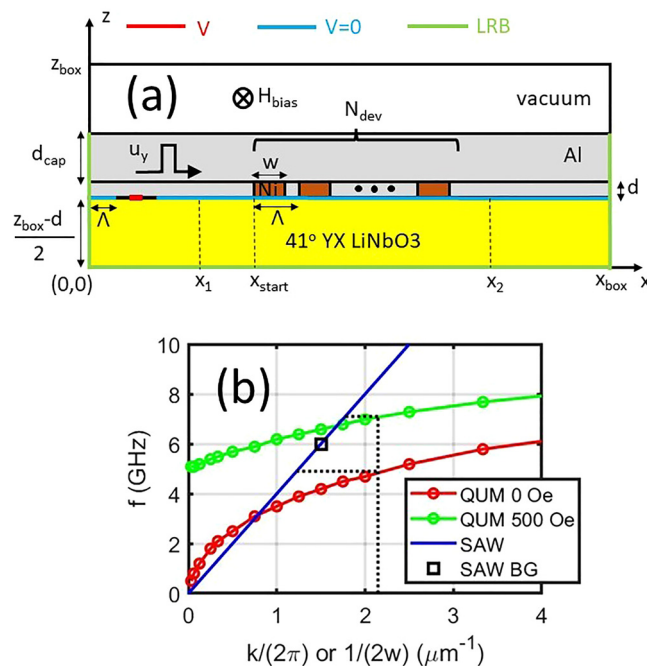

FIG. 2. (a) Geometry of the model is schematically shown. An array of N_{dev} nickel stripes (brown) with thickness d and width w is formed on 41° YX LiNbO₃ substrate (yellow). The whole sample is capped with an aluminum layer (grey) of thickness d_{cap}. A region of vacuum (white) above the Al capping layer is also included in the simulation. Periodic boundary conditions are applied in the y direction. A low reflection boundary (LRB) conditions are applied to the left, right, and bottom edges (green lines) of the sample, including the Al capping layer. The interface between the LiNbO₃ substrate and the Al layer is electrically grounded (light blue line, V = 0). An electrode pad with width $0.25\lambda_d$ (red line, V) is formed on the far-left side of the LiNbO₃ substrate and is separated from the ground surface by $0.25\lambda_d$ wide gaps on each side of the pad. (b) The linear dispersion relation of Love SAWs is shown for the phase velocity of 4 μm/ns (blue straight line). The black square denotes the acoustic bandgap at 6 GHz for an array with period $\Lambda = 333$ nm. The frequency of the lowest lying SW mode, i.e., quasi-uniform mode (QUM), of the nickel stripe is shown as a function of 1/(2w) for d = 20 nm as the red and green curves with circles correspond to the bias magnetic field H_{bias} of 0 and 500 Oe, respectively, applied along the +y direction. The vertical black dotted line indicates the 1/(2w) value for w = 233 nm. The lower and upper horizontal black dotted lines indicate the QUM frequency at w = 233 nm for H_{bias} of 0 and 500 Oe, respectively.

substrate is chosen to ensure that SAWs launched by IDT with the correct orientation on the substrate surface are predominantly Love wave (see Ref. 24 and Sec. II in the supplementary material). The geometrical parameters used in our simulations are summarized in Table S1 in the supplementary material. The periodicity of the stripe array is Λ. Figure 2(b) shows the frequencies of Love SAWs in the LiNbO₃ substrate and the lowest lying SW modes of individual isolated nickel stripes. The SAWs are assumed to have a linear dispersion and velocity of 4 μm/ns, and their frequency is plotted against the inverse wavelength $1/\lambda = k/(2\pi)$, where k is the wavenumber. Then, the assumed array period $\Lambda = 333$ nm leads to Bragg reflection of acoustic waves with wavelength $\lambda = 2\Lambda = 667$ nm and an acoustic bandgap at 6 GHz. The frequencies of the lowest lying SW modes, i.e., quasi-uniform modes (QUM), in nickel stripes of d = 20 nm are calculated using OOMMF micromagnetic software package[25] for the magnetic bias field H_{bias} of 0 and 500 Oe applied in the +y direction. The QUM frequencies are plotted against 1/(2w), since the QUM to SAW coupling is most efficient when $\lambda = 2w$. As an example, the stripe width of w = 233 nm corresponds to 1/(2w) value of 2.146 μm^{-1}. This corresponds to QUM frequencies of 4.9 and 7.1 GHz at a bias field of 0 and 500 Oe, respectively. These two frequencies correspond to SAWs with $k/(2\pi)$ values of 1.225 and 1.775 μm^{-1}, respectively, which are both smaller than the 1/(2w) value of 2.146 μm^{-1} for w = 233 nm. Therefore, the condition $k/(2\pi) < 1/(2w)$ (i.e., the SAW wavelength to be larger than twice the stripe width or $\lambda > 2w$) is satisfied for both frequencies.

In the above example, we have effectively designed a SAW metamaterial that is tunable by a magnetic field. As we increase H_{bias} from 0 to 500 Oe, the frequency of the QUM of the nickel stripe and associated resonant absorption of SAWs will continuously rise from 4.9 to 7.1 GHz. Therefore, at a certain intermediate H_{bias} value, the frequency of the maximum magnetic absorption will coincide with the acoustic band edge at about 6 GHz, which will lead to the Borrmann effect, as introduced in Sec. I. The stripe width of w = 233 nm is chosen as a compromise between retaining enough magnetic material to interact with the SAW and leaving a wide enough gap between the stripes (i.e., $\Lambda - w = 100$ nm) to reduce the inter-stripe magnetic dipolar coupling. To illustrate the enhanced interaction by the Borrmann effect, we compare the results to a continuous thin film of nickel with the same thickness d = 20 nm and the total length of $\Lambda \times N_{dev} = 6.67$ μm. In Figs. 3(a)–3(d), we present the transmission spectra of the system depicted in Fig. 2(a) for w = 333, 300, 266, and 233 nm, while array period Λ is kept constant at 333 nm. These values of w correspond to the case of a continuous film [Fig. 3(a)], two intermediate array cases [Figs. 3(b) and 3(c)], and our target designed metamaterial array [Fig. 3(d)], respectively. The methodology for the calculation of the transmission spectra is given in Sec. II in the supplementary material. The material parameters are listed in Table S4 in the supplementary material. For each value of w, we varied the bias field to 150, 250, 350, and 5 kOe accordingly.

To extract the effect of magnetoelastic coupling, we shall use the transmission spectrum at $H_{bias} = 5$ kOe as a reference. Indeed, for such bias field, the frequencies of the magnetic modes are expelled far above the band of interest and cannot be excited acoustically, so that all the features in the spectrum are of purely

mechanical origin. For the case of a continuous film [Fig. 3(a)], we see that the SAWs are fully transmitted, i.e., $|S_{21}| = 0$ dB. When w is reduced to 300 nm, i.e., when the gaps between neighboring stripes are small, a shallow transmission dip centerd at 6.5 GHz appears in the spectrum [Fig. 3(b)]. This dip deepens and expands when w is further reduced, while its frequency position is downshifted to 6 GHz [Figs. 3(c) and 3(d)], which corresponds to the aforementioned acoustic bandgap in Fig. 2(b).

Let us now consider the case of coupled magneto-elastic dynamics, when the QUM frequency is comparable to that of the acoustic bandgap, which occurs when H_{bias} is lowered. As shown in Fig. 3(a), as H_{bias} is set to 150, 250, and 350 Oe, the transmission spectrum exhibits an attenuation dip (relative to the pure mechanical background at 5 kOe) shifting toward higher frequencies as H_{bias} is increased. This corresponds to the case of attenuation of Love SAWs due to coupling with the Damon–Eshbach spin waves in the continuous nickel film, as experimentally studied recently.[14] In our study, for a total film length of 6.67 μm, the attenuation is −5 dB at $H_{bias} = 150$ Oe, increasing to −7 dB at $H_{bias} = 250$ and 350 Oe. This yields attenuation rates of −0.75 and −1.05 dB/μm, respectively. These figures give the baseline for

evaluation of the performance of the metamaterial array. When w is reduced to 300 nm, the transmission spectra at $H_{bias} = 150$, 250, and 350 Oe are altered significantly [Fig. 3(b)], in comparison to the case of the continuous film, Fig. 3(a): there is a moderate reduction in depth of maximum attenuation and a shift in its frequency position. In what follows, we shall discuss the results in terms of "relative attentuation," that is, attenuation at a given low bias field relative to the reference background at 5 kOe. This reduction in the relative attenuation continues in case of w = 266 nm [Fig. 3(c)] and w = 233 nm [Fig. 3(d)]. In the case of the targeted metamaterial array [Fig. 3(d)], the relative attenuations are so shallow (smaller than −3 dB) and flat against the frequency for the three low bias field values that the attenuation maximum is no longer discernible. We note that when w is decreased and the acoustic bandgap is formed at 6 GHz, the attenuation of transmission at low bias fields develops a sharp dip. This feature is mostly insensitive to the bias field and matches the dip in the purely mechanical background. However, after the purely mechanical background is subtracted, the resulting magnetic contribution is weak and shallow in the case of the metamaterial array [Fig. 3(d)] as compared to the case of the continuous film
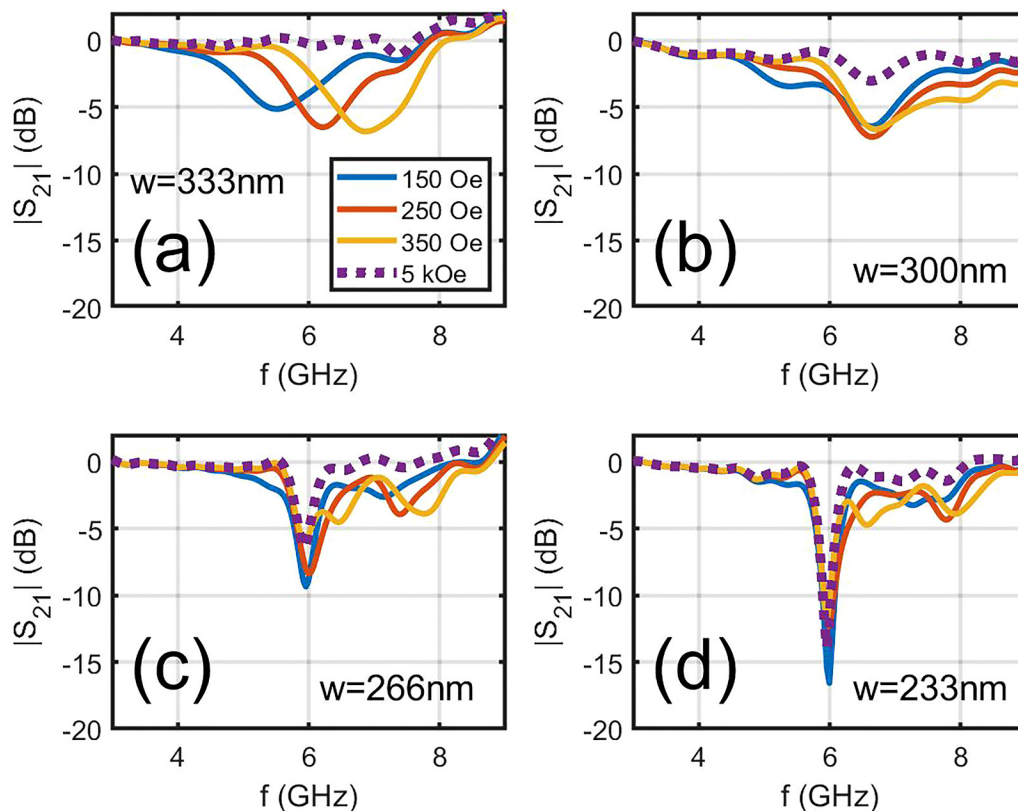
FIG. 3. Transmission spectra of the single layer nickel array depicted in Fig. 2 for (a) w = 333, (b) 300, (c) 266, and (d) 233 nm. Array period Λ is kept constant at 333 nm for (a)–(d). For each case of w, the bias field H_{bias} is set at 150 Oe (solid blue curve), 250 Oe (solid red curve), 350 Oe (solid yellow curve), and 5 kOe (dotted purple curve), respectively.

[Fig. 3(a)]. (The phase of the transmission spectra that correspond to the data in Fig. 3 is displayed in Fig. S2 in the supplementary material.) The corresponding magnitude and phase of the reflection are displayed as Figs. S3 and S4 in the supplementary material, respectively. The expected enhancement of interaction between SAW and magnetic resonance due to Borrmann effect is not observed. The main culprit that leads to this result is the nickel's Gilbert damping factor, which was set to the standard literature value of 0.038 (see Table S4 in the supplementary material). If the magnetic material is too lossy, the excited magnetic resonance may not undergo enough cycles of oscillation to produce enough Bragg reflections for the Borrmann effect to occur.

To verify that the SAW propagates far enough through the array to produce the coherent interference that leads to the Borrmann effect, we repeat the analysis for a more optimistic damping factor of 0.01 for the metamaterial. The results are displayed in Figs. 4(a)–4(f). First, in Figs. 4(a)–4(f), the same set of
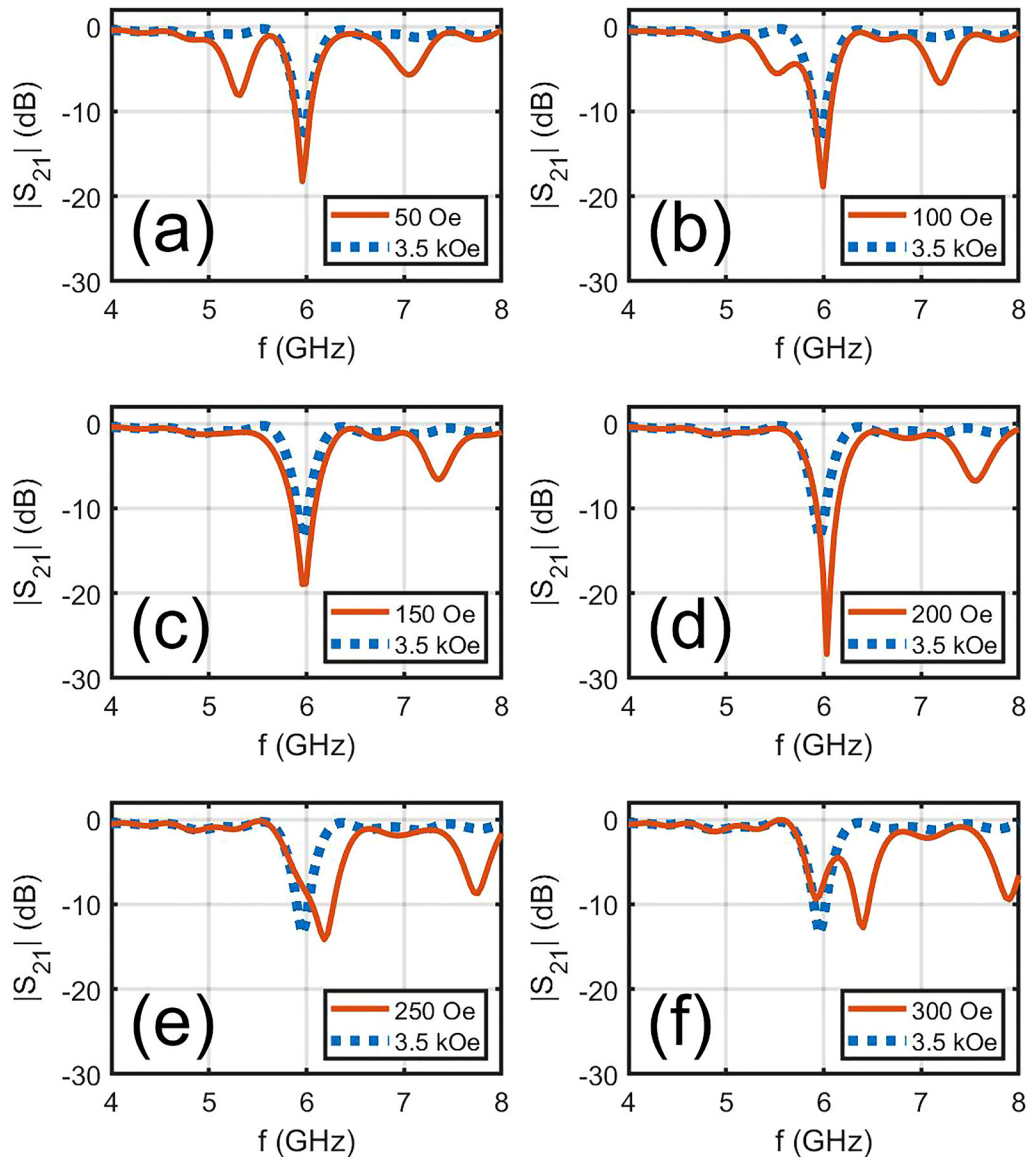
FIG. 4. (a)–(f) Simulated transmission for the designed single layer nickel array metamaterial (w = 233 nm) with nickel Gilbert damping factor lowered to 0.01. The H_{bias} is increased from 50 to 300 Oe from (a) to (f) (brown curves). Also in each graph, the same pure mechanical transmission background calculated by applying a saturating bias field at 3.5 kOe is being plotted (dotted blue curves) for the purpose of comparison.

19 December 2023 14:32:54

transmission data of pure mechanical response produced by applying the bias field at 3.5 kOe is plotted (dotted blue curves). A single sharp transmission dip at 6 GHz corresponds to the expected acoustic bandgap. In Fig. 4(a), two relative transmission dips appear at 5.31 and 7.02 GHz for $H_{bias} = 50$ Oe (brown curve). To understand the nature of these two magnetic resonances, we perform spatially resolved Fourier transform of the magnetization precession component, and the results are displayed in Fig. S5 in the supplementary material. It is identified that the resonance at 5.31 GHz is the QUM with uniform precession phase within each magnetic stripe, while the resonance at 7.02 GHz is the "dark mode": each nickel stripe is split horizontally into two half-regions that precess in opposite phases. In this article, we focus our attention only on the QUM since this is the mode we intend to tune using H_{bias} [see Fig. 2(b)]. The frequency of the dark mode (7.02 GHz) is already way above the acoustic bandgap at 6 GHz when $H_{bias} = 50$ Oe, and there is no way to move the mode across the acoustic bandgap by further increasing the H_{bias}.

We now try to slowly sweep the QUM across the acoustic bandgap in the transmission spectrum by increasing frequency of the QUM. This is achieved by increasing the H_{bias} field value from 50 to 300 Oe in steps of 50 Oe [Figs. 4(a)–4(f)]. For each H_{bias} value, we can identify the QUM attenuation dip frequency, attenuation maximum, attenuation of the mechanical background at the same frequency, and, therefore, the relative attenuation by subtracting the QUM attenuation maximum with the mechanical background. The results are summarized in Table I. We find that at $H_{bias} = 50$ Oe, the QUM resonant frequency is much smaller than that of the lower bandgap edge [Fig. 4(a)], and the relative attenuation is at -7.2 dB (Table I). The relative attenuation is then suppressed to -5.2 and -5.5 dB when H_{bias} is increased to 100 and 150 Oe (Table I), at which the QUM is now approaching and overlapping with the acoustic bandgap [Figs. 4(b) and 4(c)]. As H_{bias} is further increased to 200 Oe, the relative attenuation is increased to -18.2 dB (Table I). This happens when the QUM is located at the upper edge of the acoustic bandgap [Fig. 4(d)]. As we increase H_{bias} to 250 and 300 Oe, the QUM frequency increases and exits the bandgap [Figs. 4(e) and 4(f)], and the relative attenuation is moderately reduced to -12.0 and -12.3 dB (Table I).

To understand the dependence of relative attenuation against the relative position of the QUM to the acoustic bandgap, we

consider the attenuation mechanism of the Love SAWs. In our case, the static magnetization in the stripes is aligned in the +y direction, so that its unit vector is given by $(m_x, m_y, m_z) = (0,1,0)$. Then, as we show in the supplementary material [see Eq. (S9)], the SAW is attenuated by exciting the magnetic resonance through the x component of the magnetoelastic field given by $H_{mel,x} = -2B_2\varepsilon_{xy}/(\mu_0 M_s)$. In Fig. 5, the Fourier transform of the strain tensor xy component ($\mathcal{F}\{\varepsilon_{xy}\}$) at the QUM frequency is plotted against x for all previous values of H_{bias} in Fig. 4 and Table I. We see that at $H_{bias} = 100$ Oe, where the QUM is entering the acoustic bandgap [Fig. 4(b)], the magnitude of Fourier transform of strain $\varepsilon_{xy}(|\mathcal{F}\{\varepsilon_{xy}\}|)$ exhibits peaks that align with the gaps between stripes [Fig. 5(b)]. This is especially obvious in the region of x between 10 and 13 μm. Therefore, the SAW at this particular H_{bias} value excites the QUM less efficiently, and the relative attenuation is suppressed (Table I). On the other hand, at $H_{bias} = 200$ Oe where the QUM is aligned with the upper acoustic band edge [Fig. 4(d)], the peaks of the ε_{xy} Fourier transform magnitude ($|\mathcal{F}\{\varepsilon_{xy}\}|$) occur inside the magnetic stripes themselves [Fig. 5(d)]. Therefore, at this value of H_{bias}, the SAW excites the QUM more efficiently than in the case of the continuous thin film, and this yields a stronger relative attenuation (Table I). In fact, the formation of these peaks of strain tensor magnitude indicates the onset of standing waves inside the array structure and is the manifestation of the Borrmann effect (Fig. 1). At bias field value where the QUM is outside the bandgap (i.e., $H_{bias} = 50$, 250, and 300 Oe), the SAWs are largely travelling wave inside the array structure. In these cases, the strain magnitude $|\mathcal{F}\{\varepsilon_{xy}\}|$ is relatively position independent (instead of forming peaks) and phase $\angle\mathcal{F}\{\varepsilon_{xy}\}$ decreases steadily with x [Figs. 5(a), 5(e), and 5(f)]. Therefore, at these bias field values, the ability of SAWs to excite the QUM is at an intermediate level, which results in intermediate values of the relative attenuation (Table I).

So far we have been discussing the subject in terms of S_{21} against frequency. In order to offer a perspective in the momentum space, the dispersion relation of the single-layer nickel array for various values of w and H_{bias} has been computed, and the results are displayed in Fig. 6. The results in Fig. 6(a) correspond to the case of a continuous nickel film with $H_{bias} = 5$ kOe (no magnetic response in the frequency range of interest), where a straight line of frequency against k for Love SAW is observed. After lowering H_{bias} to 50 Oe, hybridization of the SAW with magnetic resonance is seen at roughly 4.6 GHz, indicated by the occurrence of a gap with slight bending of the SAW dispersion line near to the gap edge [Fig. 6(b)]. In Fig. 6(c), the stripe width w is decreased to 233 nm, which leads to the opening of an acoustic stop band at 6 GHz as mentioned earlier. Figure 6(d) depicts the situation where the acoustic bandgap at 6 GHz coexists with SAW hybridizations with magnetic resonance at 5.3 and 7.0 GHz (quasi-uniform and dark magnetic mode). When H_{bias} is increased to 250 and 350 Oe, the quasi-uniform mode frequency is upshifted to the upper acoustic band edge and above, as indicated by the movement of the hybridization discontinuity to somewhere above the acoustic bandgap at 6 GHz [Figs. 6(e) and 6(f)].

To summarize this section, when the Gilbert damping factor is reduced to a low enough value (0.01), the metamaterial formed by an array of magnetic stripes exhibits the Borrmann effect, which enhances the coupling between a propagating

TABLE I. Frequency and transmission values extracted from Fig. 4.

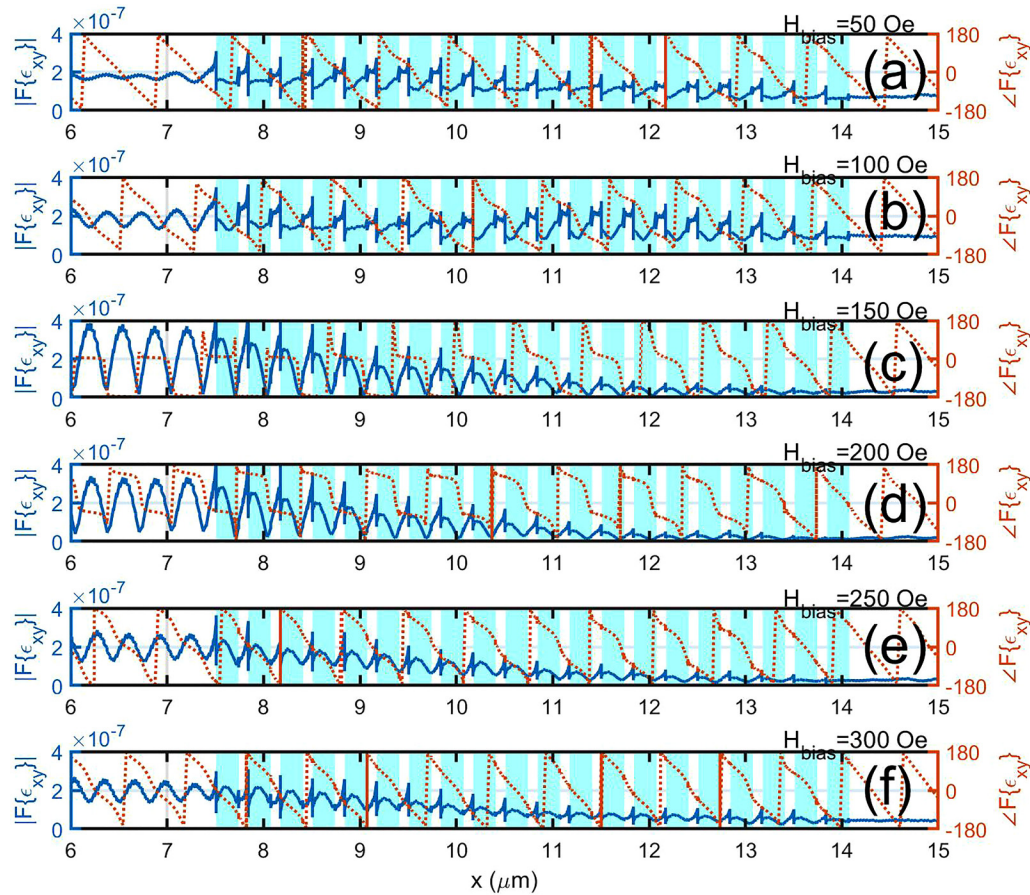| H_{bias} (Oe)	QUM frequency (GHz)	$|S_{21}|$ at QUM resonance (dB)	$|S_{21}|$ of mechanical background	Relative attenuation (dB)
50	5.32	-8.1	-0.9	-7.2
100	5.51	-5.5	-0.3	-5.2
150	5.96	-19.0	-13.5	-5.5
200	6.03	-27.2	-9.0	-18.2
250	6.18	-14.2	-2.2	-12.0
300	6.41	-12.8	-0.5	-12.3

19 December 2023 14:32:54

FIG. 5. Magnitude and phase of Fourier transform of the xy component of the strain tensor (ε_{xy}) against x for the case of broadband Love SAW pulse scattering with the single-layer nickel stripe array at QUM resonance frequency (f_{res}) for applied bias field H_{bias} equal (a) 50, (b) 100, (c) 150, (d) 200, (e) 250, and (f) 300 Oe, respectively. The notation $\mathcal{F}\{\}(f)$ denotes Fourier transform from time to frequency domain, in which the quantity's phase and magnitude are then evaluated at the QUM resonance frequency $f_{res} = 5.32$, 5.51, 5.96, 6.03, 6.18, and 6.41 GHz and are displayed as a function of position x from (a) to (f), respectively. Light blue background columns denote the position of the nickel stripes. The strain tensor is defined according to Eq. (S10) in the supplementary material and is outputted directly from COMSOL software. The corresponding u_y is being shown in Fig. S9 in the supplementary material.

SAW and the stripes' local magnetic resonance. However, this enhancement happens only at the acoustic band edge, where substantial mechanical attenuation background has occurred already (−9.0 dB at 6.03 GHz, see Table I). This mechanical background attenuation is a result of the spatial modulation of elastic properties induced at the surface by the stripe array and is, therefore, fixed when the array is fabricated. From an application point of view, this frequency overlap of the enhancement of tunable attenuation and a substantial non-tunable attenuation background is highly unfortunate. Indeed, the merit of a tunable attenuator depends not only on its maximum attenuation ability but also on the insertion loss when it is in the "pass" state: the smaller is this insertion loss, the better is the device would be. In Sec. III, we explore whether it is possible to use the Borrmann effect for attenuation enhancement when the QUM is far away from the non-tunable acoustic bandgap.

III. DOUBLE-LAYER STRIPE ARRAYS

The presence of nickel stripes on the LiNbO$_3$ surface produces both an elastic impedance mismatch and a magnetoelastic coupling for the propagating SAWs. Therefore, from the SAW's perspective, the magnetic scattering sites always coincide with the elastic ones (and have the same periodicity), which leads to the finding in Sec. II that the magnetic Borrmann effect occurs only at edges of the acoustic bandgaps. This can be overcome in a metamaterial in which the magnetic period differs from the mechanical one, e.g., in an array in which the magnetoelastic coupling is altered for every other stripe. As a result, the magnetic Bragg scattering would occur at half the frequency of the acoustic bandgap. This would allow one to achieve magnetic scattering with its strength enhanced by the spatial periodicity at frequencies within an allowed acoustic band. The natural possibility to control locally the magnetoelastic
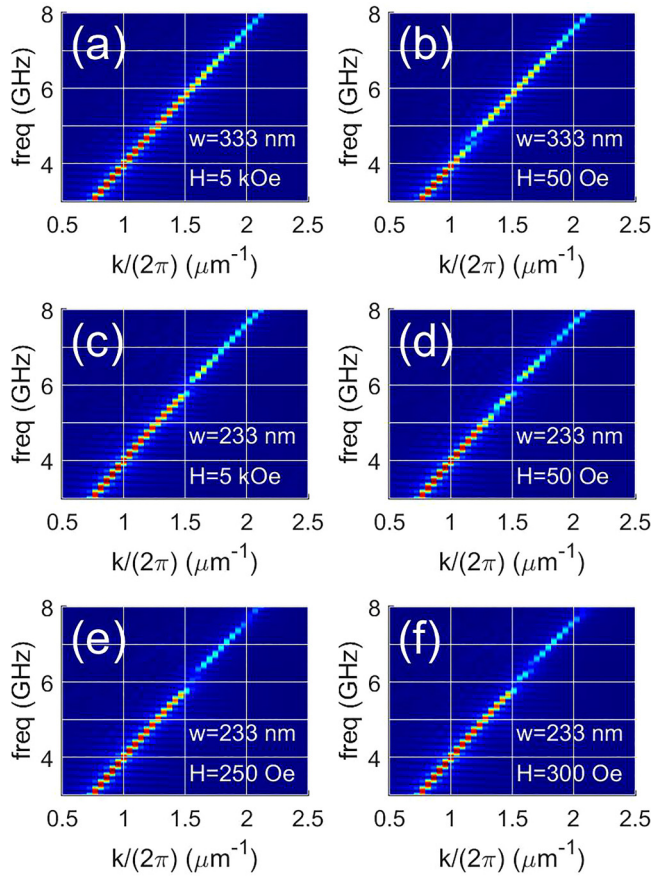
FIG. 6. (a)–(f) Dispersion relation for various values of w and H_{bias} in the single-layer nickel array with nickel Gilbert damping factor set to 0.01. The results were obtained by 2D Fourier transform of u_y (mechanical displacement in the y direction) against position (x) and time (t) to momentum (k) and frequency (f) domain under the broadband pulse excitation as described in the supplementary material Sec. II. In the simulation, N_{dev} is increased to 64. In (a)–(f), it is the absolute value of the Fourier transformed results being displayed.
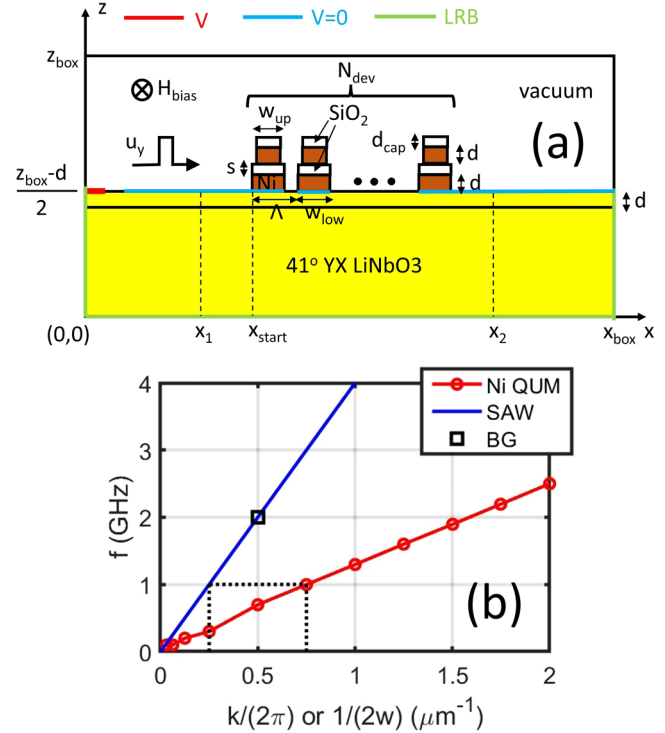

FIG. 7. (a) Schematic illustration of the double-layer nickel stripe array and the simulation setup. Details of dimension values in the figure could be found in Table S5. Notice that unlike the situation as in Fig. 2(a), the substrate surface inside the gaps between adjacent double layer stripes are not electrically grounded (i.e., the light blue lines V = 0 are discontinued inside the gaps). On the other hand, the horizontal centers of the upper and lower layers in each stripe are aligned. (b) The dispersion relation of the Love SAW is approximated as a blue straight line with phase (group) velocity equal to 4 μm/ns. The acoustic bandgap created by the array with period $\Lambda = 1$ μm is at 2 GHz, denoted by the black square. The frequency of the magnetic out of phase mode in the nickel double-layer stripe against 1/(2w), where w is the stripe width and with thickness d = 30 nm and spacing between layer s = 15 nm under a zero bias magnetic field with magnetization in anti-parallel state is plotted as red circles and red solid line. The right vertical dotted black lines indicate the value of 1/(2w) at w = 667 nm. The horizontal black dotted line indicates the frequency of the Love SAW that the out-of-phase mode at w = 667 nm is coupling to (1 GHz). The left vertical black dotted line indicates the k/(2π) value of the SAW at 1 GHz (0.25 μm⁻¹).

coupling is by reversing the magnetization in the stripe and thereby switching the precession chirality of the QUM. Then, the match or mismatch between chiralities of the QUM and the magnetoelastic field produced by the Love SAW would affect the coupling efficiency between them. In extreme circumstances where both the QUM precession and the Love SAW magnetoelastic field rotation are engineered to be completely circular in the x–z plane, this chirality mechanism could completely switch on and off the coupling between the QUM and the SAW.

Here, we go further and replace the single-layer stripes in Sec. II with double-layer stripes. The double-layer structure relies on the change of parity of the magnetoelastic field on the upper and lower layers upon magnetization reversal to control the SAW coupling to the out-of-phase magnetic mode in the double-layer stripe, thus achieving the aforementioned objective to locally control the

magnetoelastic coupling. In particular, the double-layer structure with antiparallel alignment of the layers' magnetizations can be considered as a prototypical synthetic antiferromagnet. Figure 7(a) illustrates the design of the double-layer nickel stripe array metamaterial. The array periodicity $\Lambda = 1$ μm creates an acoustic bandgap at $\lambda = 2$ μm or k/(2π) = 0.5 μm⁻¹, which correspond to a frequency f = 2 GHz indicated as the small black square in Fig. 7(b). If only every other double-layer stripe interacts magnetically with the SAW, it should induce a magnetic bandgap at $\lambda = 4$ μm or k/(2π) = 0.25 μm⁻¹ translated to frequency f = 1 GHz, as indicated by the left vertical and horizontal black dotted lines in Fig. 7(b),

19 December 2023 14:32:54

respectively. Using OOMMF, we calculate the frequency of the out-of-phase (also known as "optical") mode of the nickel double layer in antiparallel magnetization state as a function of stripe width w with spacing between layers s = 15 nm. The resultant frequencies are plotted as red circles and red line in Fig. 7(b) as a function of 1/(2w). The right vertical black dotted line indicates that the SAW at 1 GHz couples to the double-layer stripe with 1/(2w) equal 0.75 μm^{-1} or w = 667 nm, which is indeed smaller than the array period Λ (=1 μm). One should notice that this is made possible only because of the use of the double-layer stripe. In the case of a single-layer stripe, the 1 GHz SAW couples to the stripe with 1/(2w) = 0.1 μm^{-1} [see red curve in Fig. 2(b)], which corresponds to a stripe width w = 5 μm, a value that is larger than the array period Λ (= 1 μm). This highlights the capability of the double-layer design to operate at the same frequencies and with smaller stripe width than the single-layer design. The double layer with interlayer spacing s = 15 nm allows the magnetizations of the two layers to have independent static orientations but to interact dynamically through dipolar fields, forming the out-of-phase mode at a much lower frequency than the QUM in the case of single-layer stripes.

To characterize this design, we shall consider four different configurations of magnetization and applied field, as depicted in Fig. 8 and dubbed as (a) "saturated state," (b) "fully parallel state," (c) "partially antiparallel state," and (d) "fully antiparallel state." The different remanent states in (b), (c), and (d) can be achieved by an appropriate history of the bias field application. The stripes can be engineered to have different reversal magnetic field by designing the stripe ends to be pointy, square, or be connected to a domain wall injection pad (not shown). These different designs of stripe ends will result in different domain wall nucleation field and, therefore, different stripe magnetization reversal field by domain
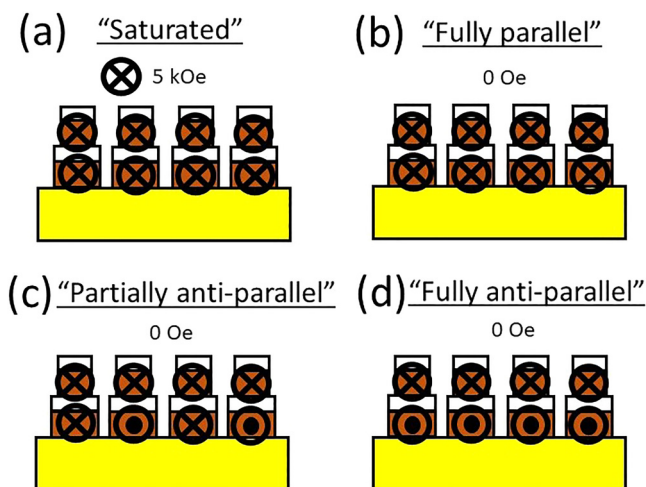

FIG. 8. Four different states of magnetization and applied bias field. The circle cross (dot) symbol indicates magnetization or bias field pointing toward the positive (negative) y direction in Fig. 7. In each case, only four stripes are shown, but the rest of the array follows the same pattern.

wall motion through the stripes. The smaller width of the stripe's upper layer also makes reversing its magnetization harder as compared to the lower layer. In our design, we set the upper and lower layers' widths to be w_{up} = 650 nm and w_{low} = 750 nm, respectively (Table S5 in the supplementary material). This is partially for the two layers to have different reversal fields and partially to simplify their lithography, practically. The modification of the stripe width to be unequal on the upper and lower layers will change the out-of-phase mode frequency. However, it can be easily shifted back to the original target value of 1 GHz by tuning the spacer layer thickness s to 16.5 nm (Table S5).

The magnetic mode profile of the stripe array under broadband Love SAW pulse excitation for the four magnetic configurations as depicted in Fig. 8 is plotted for the lower layer (Fig. 9) and upper layer (Fig. 10) of the stripes, respectively. The occurrence of a "bump" of $|\mathcal{F}\{m_x\}|$ inside a stripe in Figs. 9 and 10 implies that the magnetic mode at 1 GHz inside that particular stripe has been "switched on," and the stripe contributes to the absorption of the SAW's energy. By comparing Figs. 9 and 10 with Fig. 8, one can conclude that the magnetic mode at f = 1 GHz is excited by the SAW pulse if and only if the corresponding double-layer stripe is in an antiparallel magnetization state. On the other hand, in each stripe of Figs. 9 and 10 where the 1 GHz mode has been excited, the phases in the upper layer (Fig. 9) and in the lower layer (Fig. 10) are 180° shifted relative to each other, indicating this mode to be an "out-of-phase" mode. We note that in the antiparallel magnetization state, the m_x components in the two layers are out of phase while their m_z components are in phase. However, because of the shape anisotropy of the stripe cross section, the magnetization is highly elliptical with amplitude of m_x dominating compared to m_z, and so, the term "out-of-phase" remains justified.

The reason why the out-of-phase mode at 1 GHz is excited if and only if the double-layer stripe is in an antiparallel state is as follows. As we show in the supplementary material [see Eq. (S9)], the magnetoelastic field that excites the mode is given by $H_{mel,x} = -2B_2\varepsilon_{xy}m_y/(\mu_0 M_s)$. Therefore, when the magnetization in a layer is switched from +y to −y direction, m_y switches from +1 to −1, and $H_{mel,x}$ changes sign while retaining its magnitude. A double layer with parallel (antiparallel) magnetization alignment has an even (odd) parity of $H_{mel,x}$ upon the upper and lower layers. On the other hand, since the 1 GHz out-of-phase mode has odd parity of phase upon the lower and upper layers, only a $H_{mel,x}$ field with odd parity upon the same two layers can excite the mode. Therefore, excitation of this "out-of-phase" mode at 1 GHz requires the double layer to be in the antiparallel state.

The opportunity to switch on and off the coupling between the SAW and the magnetic mode by controlling the magnetization state of the double layer gives us a unique opportunity to reconfigure the spatial periodicity of the magnetic interaction with the SAW. One can observe that in the "partially antiparallel" state, the SAW interacts with the 1 GHz out-of-phase mode with a spatial periodicity that is twice the array periodicity [Figs. 9(c) and 10(c)]. As we have discussed earlier in this section, this would lead to a Bragg reflection at a frequency that is in the middle of the acoustic passband. Indeed, this is what we observe from the simulation. Figure 11(a) depicts the reflection coefficient against frequency for the four magnetic states shown in Fig. 8. While all four states show
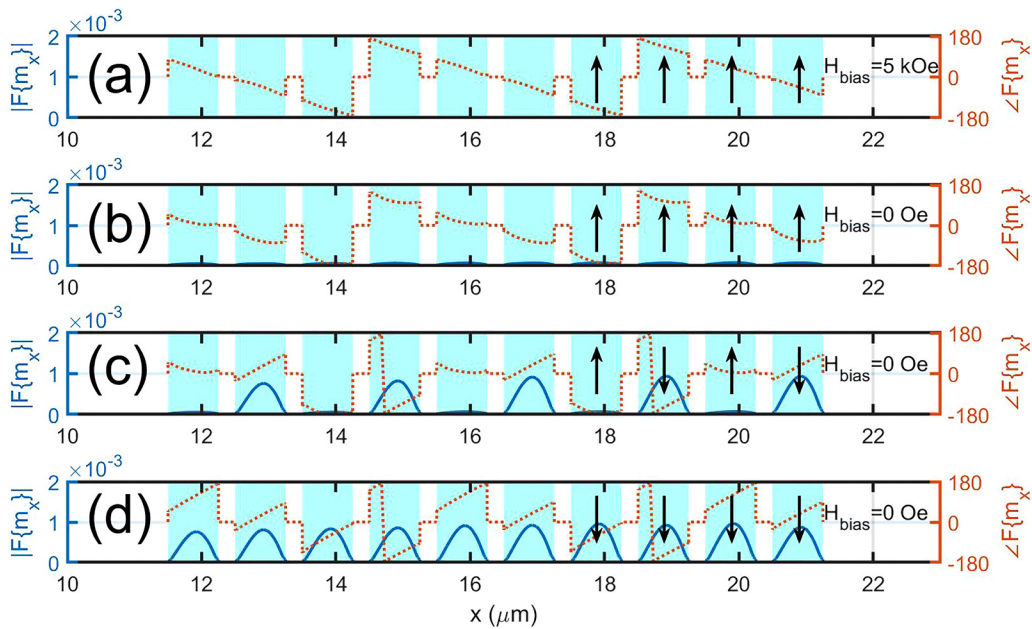
FIG. 9. Magnitude (blue solid curve) and phase (brown dotted curve) of the Fourier transform (from time to frequency) of the x component of the precession magnetization ($F\{m_x\}$) at frequency $f = 1$ GHz for the lower layer of the double-layer nickel stripe array as a function of x for the case of (a) saturated state, (b) fully parallel state, (c) partially anti-parallel state, and (d) fully anti-parallel state depicted in Fig. 8. The light blue background columns depict the position of the stripes. The arrows in the four stripes nearest to the right show the static magnetization direction in the corresponding stripe with upward (downward) arrow as magnetization pointing toward the positive (negative) x direction. Magnetization direction in the rest of the stripes that are not indicated with any arrows could be deduced by the same pattern accordingly. The stripes mentioned here are always referring to those in the lower layer of the double layers.
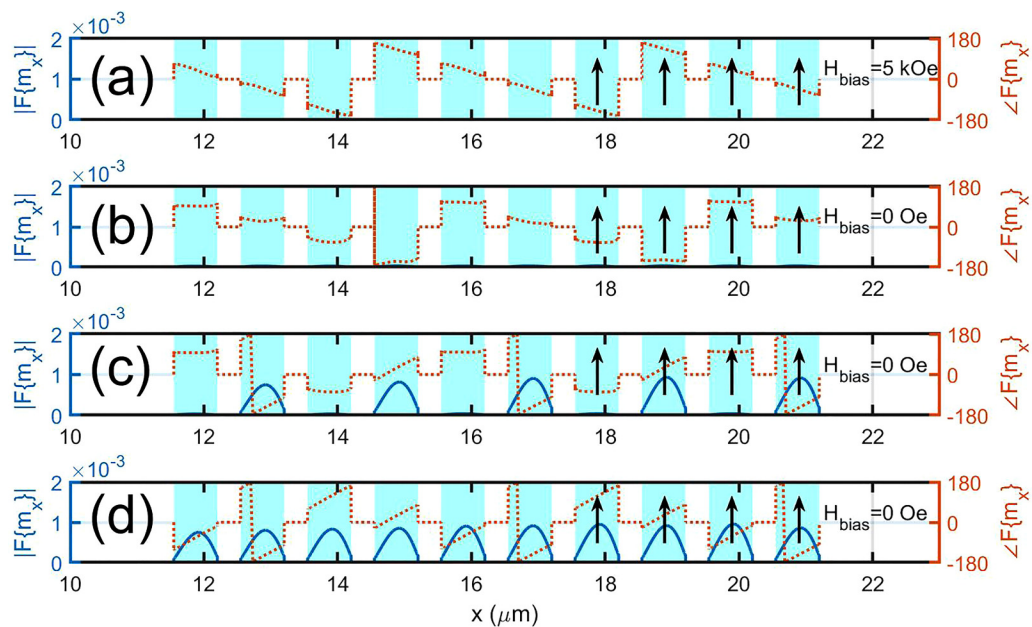

FIG. 10. Identical to those of Fig. 9 except it is the upper layer being shown instead of the lower layer.
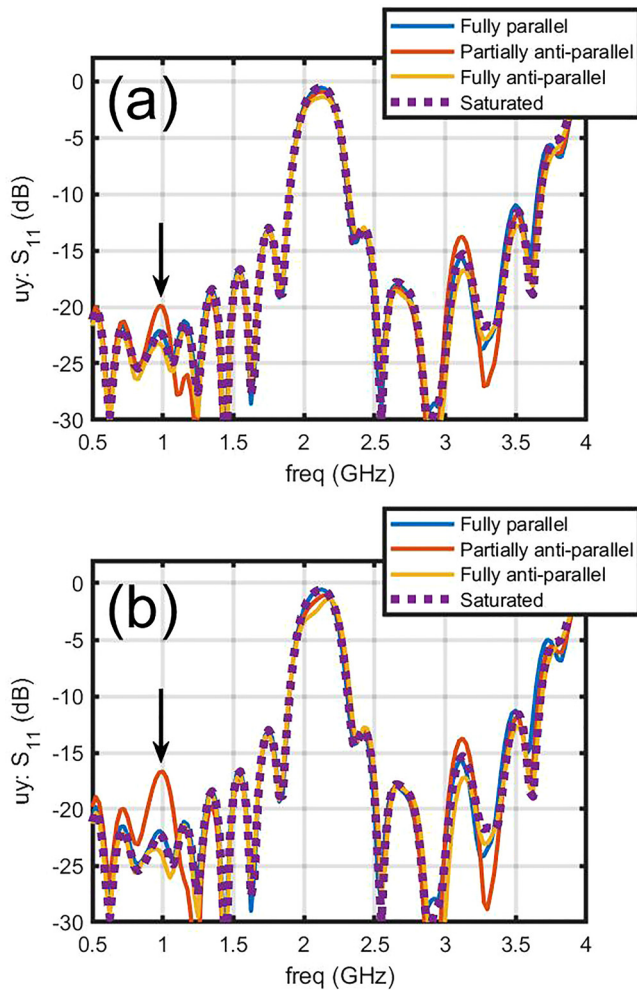
19 December 2023 14:32:54

FIG. 11. Calculated SAW magnitude of the reflection coefficient spectrum of the double-layer nickel stripe array for the four states of magnetization and applied bias field depicted in Fig. 8. The nickel Gilbert damping factor is kept at 0.038 in (a) and reduced to 0.01 in (b). The arrows indicate the peaks that correspond to pure magnetic Bragg reflection.

FIG. 12. Calculated SAW magnitude of the transmission coefficient spectrum of the double-layer nickel stripe array for the four states of magnetization and applied bias field depicted in Fig. 8. The nickel Gilbert damping factor is kept at 0.038 in (a) and reduced to 0.01 in (b). The attenuation dip near to 3 GHz in (a) and (b) corresponds to excitation of higher order magnetic mode in the stripes depicted in Fig. S11, which is outside the scope of this article.

a common strong reflection peak near 2 GHz, which corresponds to the acoustic Bragg reflection, only in the case of the "partially antiparallel" state (brown solid curve), there is a reflection peak at 1 GHz, as highlighted by the downward black arrow. This purely magnetic reflection peak stands 2 dB above the noise floor created by the other three magnetic states (blue and yellow solid curve and purple dotted curve). Notably, the data presented in Fig. 11(a) are computed assuming a standard nickel Gilbert damping factor of 0.038. The magnetic Bragg reflection peak becomes even more prominent after this damping factor is lowered to 0.01 as depicted in Fig. 11(b), again as indicated by the downward black arrow. Now the magnetic reflection peak stands above the noise floor by 5 dB.
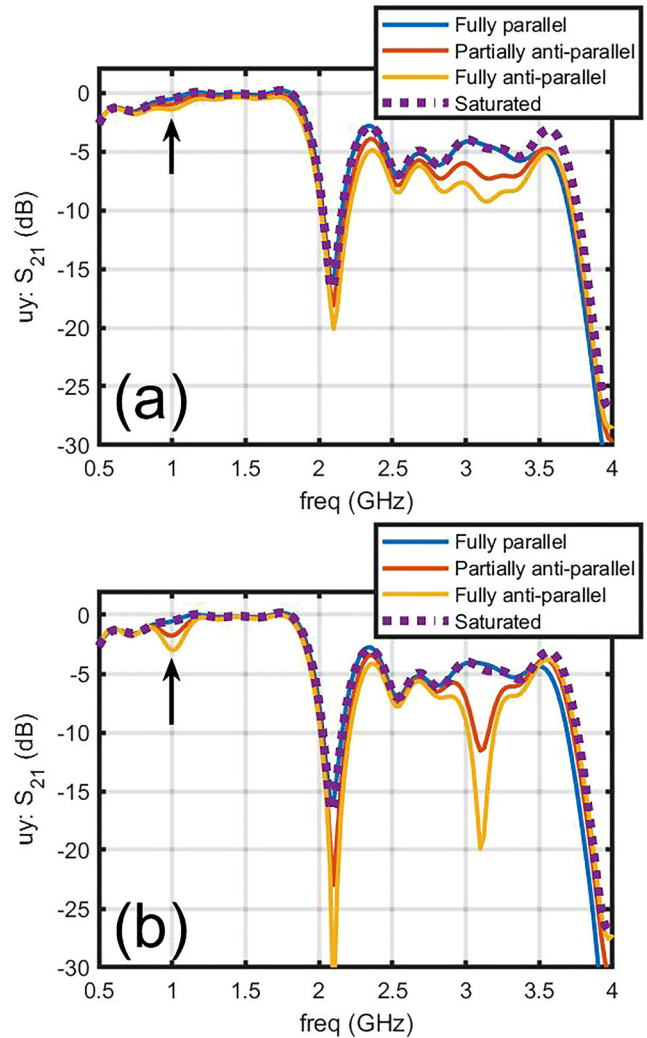
Hence, we have verified the existence of a new magnetoacoustic feature in the reflection spectrum at a frequency far away from the acoustic Bragg reflection. This reflection peak arises because of the spatial periodicity of the SAW interaction with the magnetic modes. Let us now inspect whether the Borrmann effect, i.e., enhancement of magnetoacoustic interaction, occurs in the transmission spectrum at the frequency of this reflection peak. The transmission spectra shown in Fig. 12 were obtained for the same condition as the reflectance spectra in Fig. 11. We observe in Fig. 12(a) that the transmission spectra for all four magnetic states (Fig. 8) exhibit a common dip near 2 GHz. This dip is the acoustic

19 December 2023 14:32:54

bandgap created by the periodicity of the array. On the other hand, the fully antiparallel state (yellow solid curve) and the partially antiparallel state (brown solid curve) exhibit a very shallow recess at 1 GHz (indicated by the upward black arrow) in comparison to the fully parallel state (blue curve) or the saturated state (purple dotted curve) as baseline. This small recess grows into observable dips when the nickel Gilbert damping factor is lowered to 0.01, as shown in Fig. 12(b) and as indicated again by an upward black arrow. The partially antiparallel state (brown solid curve) and fully parallel state (yellow solid curve) exhibit a dip at 1 GHz with attenuation depth of roughly −1 and −2 dB relative to the background provided by the fully parallel state (blue solid curve) and saturated state (purple dotted curve), respectively.

Certainly, switching of a double-layer stripe into the antiparallel state activates its coupling of the 1 GHz out-of-phase mode to the acoustic waves, which is responsible for the attenuation dips at 1 GHz in the SAW transmission spectra of Figs. 12(a) and 12(b). However, the crucial question is whether this interaction is enhanced by the spatial periodicity of the magnetic scattering sites. The number of antiparallelly aligned stripes in the fully antiparallel state is twice the number of those in the partially antiparallel state, as depicted in Fig. 8. At 1 GHz, the corresponding $k/(2\pi)$ value for the Love SAW is $0.25\,\mu m^{-1}$ [Fig. 7(b) blue line]. The magnetic scattering site periodicity for the partially antiparallel state is 2Λ, i.e., $2\,\mu m$, which translates to a $k/(2\pi)$ value equal $0.5\,\mu m^{-1}$, which is twice that of the Love SAW at 1 GHz ($0.25\,\mu m^{-1}$). Therefore, in the case of the partially antiparallel state, the Bragg condition corresponds to the spatial periodicity of the magnetic scattering sites, and the magnetoelastic interaction due to this periodicity should be enhanced. Following the same arguments, one can deduce that the Bragg condition is not satisfied at 1 GHz in the case of the fully antiparallel state, and one should not expect the spatial periodicity of this state to enhance magnetoelastic interaction. The number of active magnetic scattering sites in the partially antiparallel state is half of those in the fully antiparallel state. Therefore, a coherent enhancement of the magnetoelastic interaction for the partially antiparallel state should manifest itself as a relative attenuation depth larger than half of that in the fully antiparallel state. However, as we have seen in Fig. 12(b), the partially antiparallel state relative attenuation depth at 1 GHz is almost exactly half of the one for the fully antiparallel state (i.e., −1 dB vs −2 dB). So, we must conclude that the transmission spectrum does not reveal any significant enhancement of magnetoelastic interaction due to coherent Bragg scattering, even when the value of the Gilbert damping factor is lowered to 0.01.

IV. DISCUSSION

In the Introduction, we have explained that the Borrmann effect leads to the modification of magnetoelastic coupling at band edges due to reduction in the group velocity and formation of a standing wave. In Sec. II, we learned that if we rely on mechanical scattering to form the required bandgap and edges, we are faced with the conundrum of having tunable attenuation enhancement only when non-tunable loss is already substantial. In Sec. III, we turned to a different strategy of relying on purely magnetic scattering to produce the required bandgap and hoping that the magnetic

origin of the resultant bandgap would also make it removable magnetically. However, the results have proven that pure magnetoelastic scattering is just too weak to produce a bandgap that could lead to any observable attenuation enhancement. This is true even if the nickel Gilbert damping factor is lowered to a moderately unrealistic value. Here, we see the flaw of relying on the Borrmann effect to improve interaction: the interaction could be further enhanced only if it is already considerably strong. The Borrmann effect could make a strong interaction even stronger but cannot render a weak interaction strong. However, our adventure in exploring the broader subject of using spatial periodicity to enhance magnetoelastic interaction (which includes the Borrmann effect) is not completely futile. In Sec. III, we did observe a purely magnetic Bragg reflection (which is tunable) at a frequency that is far away from the acoustic one (which is non-tunable). The existence of this pure magnetic reflection peak could also be seen as a form of interaction enhancement due to the spatial periodicity of scattering sites. The magnetic Bragg reflection could find its application in reconfigurable radio-frequency identification (RFID) devices,[2] where SAW reflection plays a crucial role in providing the microwave response signal to the interrogating device.

We have chosen nickel as the magnetostrictive material to construct our metamaterial because it has historically been studied intensively in the literature. However, because of the high Gilbert damping factor, nickel may not be the best material. There do exist other materials with magnetoelastic interaction strength comparable to nickel yet much less lossy.[7] The frequency engineering method demonstrated in the design of our double-layer stripe in Sec. III implies that materials such as CoFe and CoFeB, which have previously been ignored because of high frequencies of their stripe QUM, can now be reconsidered. We do not expect the findings of this article to be overthrown after nickel has been replaced, but it is certainly the way to go if phononics is to advance toward usage of magnetoelastic interaction. An exciting prospect of magneto-acoustics-based phononics is its application in reservoir computing,[26] which requires the SAW to drive the magnetic resonance into nonlinear regime. Unfortunately, this could not be achieved with nickel since it is too lossy to allow the magnetic mode to be driven into large amplitude required by non-linearity.

V. CONCLUSIONS

In conclusion, we have numerically explored the possibility of implementing magnetoelastic interaction enhancement by a Borrmann effect between Love SAWs and a metamaterial formed from an array of nickel stripes. We have found that such enhancement is possible if the nickel Gilbert damping factor is lowered to a moderately unrealistic value of 0.01. By constructing a synthetic antiferromagnet using a dipolar-coupled magnetic double layer structure, we have explored the possibility of frequency engineering of its magnetic resonance. Through manipulating the parity of the magnetoelastic field, we have also investigated a novel mechanism to switch the magnetoelastic interaction on and off by realigning the magnetizations of the double layer into parallel or anti-parallel configurations. The resultant double-layer array metamaterial structure is capable of producing pure magnetic Bragg reflection that could find its application in reconfigurable RFID. Though we have

not succeeded in achieving Borrmann effect-associated magnetoe-lastic interaction enhancement that is far away from the acoustic bandgap, our design still paves the way for such possibility once nickel is replaced by some other material that is less dissipative but has a similar magnetoelastic coupling constant. These findings would set up the stage for the development of reservoir computing based on magnetoelastic coupled SAWs.

SUPPLEMENTARY MATERIAL

See the supplementary material for the details of (i) the COMSOL finite element method simulation, (ii) methods to obtain scattering coefficients from broadband pulse excitation, and (iii) additional figures of scattering coefficients spectrum for the array structures and the associated Fourier transform generated mode profiles.

ACKNOWLEDGMENTS

AUTHOR DECLARATIONS

Conflict of Interest

The authors have no conflicts to disclose.

Author Contributions

Y. Au: Conceptualization (equal); Data curation (equal); Formal analysis (equal); Investigation (equal); Methodology (equal); Validation (equal); Visualization (equal); Writing – original draft (lead); Writing – review & editing (equal). **O. S. Latcham:** Conceptualization (equal); Writing – review & editing (equal). **A. V. Shytov:** Conceptualization (equal); Funding acquisition (equal); Project administration (equal); Supervision (equal); Validation (equal); Writing – review & editing (equal). **V. V. Kruglyak:** Conceptualization (equal); Funding acquisition (equal); Project administration (equal); Resources (equal); Supervision (equal); Validation (equal); Writing – review & editing (equal).

DATA AVAILABILITY

The data that support the findings of this study are available from the corresponding author upon reasonable request.

REFERENCES

[1]K. Nakamura, "Shear-horizontal piezoelectric surface acoustic waves," Jpn. J. Appl. Phys. **46**, 4421–4427 (2007).

[2]C. Herrojo, F. Paredes, J. Mata-Contreras, and F. Martín, "Chipless-RFID: A review and recent developments," Sensors **19**, 3385 (2019).

[3]W. Fu, Z. Shen, Y. Xu, C.-L. Zou, R. Cheng, X. Han, and H. X. Tang, "Phononic integrated circuitry and spin–orbit interaction of phonons," Nat. Commun. **10**, 2743 (2019).

[4]B. J. Shastri, A. N. Tait, T. Ferreira de Lima, W. H. P. Pernice, H. Bhaskaran, C. D. Wright, and P. R. Prucnal, "Photonics for artificial intelligence and neuro-morphic computing," Nat. Photonics **15**, 102–114 (2021).

[5]A. V. Chumak, P. Kabos, M. Wu, C. Abert, C. Adelmann, A. O. Adeyeye, J. Åkerman, F. G. Aliev, A. Anane, A. Awad, C. H. Back, A. Barman, G. E. W. Bauer, M. Becherer, E. N. Beginin, V. A. S. V. Bittencourt, Y. M. Blanter, P. Bortolotti, I. Boventer, D. A. Bozhko, S. A. Bunyaev, J. J. Carmiggelt, R. R. Cheenikundil, F. Ciubotaru, S. Cotofana, G. Csaba, O. V. Dobrovolskiy, C. Dubs, M. Elyasi, K. G. Fripp, H. Fulara, I. A. Golovchanskiy, C. Gonzalez-Ballestero, P. Graczyk, D. Grundler, P. Gruszecki, G. Gubbiotti, K. Guslienko, A. Haldar, S. Hamdioui, R. Hertel, B. Hillebrands, T. Hioki, A. Houshang, C.-M. Hu, H. Huebl, M. Huth, E. Iacocca, M. B. Jungfleisch, G. N. Kakazei, A. Khitun, R. Khymyn, T. Kikkawa, M. Kläui, O. Klein, J. W. Kłos, S. Knauer, S. Koraltan, M. Kostylev, M. Krawczyk, I. N. Krivorotov, V. V. Kruglyak, D. Lachance-Quirion, R. Lebrun, Y. Li, M. Lindner, R. Macêdo, S. Mayr, G. A. Melkov, S. Mieszczak, Y. Nakamura, H. T. Nembach, A. A. Nikitin, S. A. Nikitov, V. Novosad, J. A. Otálora, Y. Otani, A. Papp, B. Pigeau, P. Pirro, W. Porod, F. Porrati, H. Qin, B. Rana, T. Reimann, F. Riente, O. Romero-Isart, A. Ross, A. V. Sadovnikov, A. R. Safin, E. Saitoh, G. Schmidt, H. Schultheiss, K. Schultheiss, A. A. Serga, S. Sharma, J. M. Shaw, D. Suess, O. Surzhenko, K. Szulc, T. Taniguchi, M. Urbánek, K. Usami, A. B. Ustinov, T. van der Sar, S. van Dijken, V. I. Vasyuchka, R. Verba, S. Viola Kusminskiy, Q. Wang, M. Weides, M. Weiler, S. Wintz, S. P. Wolski, and X. Zhang, "Advances in magnetics roadmap on spin-wave computing," IEEE Trans. Magn. **58**, 0800172 (2022).

[6]S. Watt, M. Kostylev, A. B. Ustinov, and B. A. Kalinikos, "Implementing a magnonic reservoir computer model based on time-delay multiplexing," Phys. Rev. Appl. **15**, 064060 (2021).

[7]Y. Li, C. Zhao, W. Zhang, A. Hoffmann, and V. Novosad, "Advances in coherent coupling between magnons and acoustic phonons," APL Mater. **9**, 060902 (2021).

[8]J. Puebla, Y. Hwang, S. Maekawa, and Y. Otani, "Perspectives on spintronics with surface acoustic waves," Appl. Phys. Lett. **120**, 220502 (2022).

[9]M. Weiler, L. Dreher, C. Heeg, H. Huebl, R. Gross, M. S. Brandt, and S. T. B. Goennenwein, "Elastically driven ferromagnetic resonance in nickel thin films," Phys. Rev. Lett. **106**, 117601 (2011).

[10]S. Tateno and Y. Nozaki, "Highly nonreciprocal spin waves excited by magnetoelastic coupling in a Ni/Si bilayer," Phys. Rev. Appl. **13**, 034074 (2020).

[11]C. Zhao, Y. Li, Z. Zhang, M. Vogel, J. E. Pearson, J. Wang, W. Zhang, V. Novosad, Q. Liu, and A. Hoffmann, "Phonon transport controlled by ferromagnetic resonance," Phys. Rev. Appl. **13**, 054032 (2020).

[12]M. Xu, K. Yamamoto, J. Puebla, K. Baumgaertl, B. Rana, K. Miura, H. Takahashi, D. Grundler, S. Maekawa, and Y. Otani, "Nonreciprocal surface acoustic wave propagation via magneto-rotation coupling," Sci. Adv. **6**, eabb1724 (2020).

[13]P. J. Shah, D. A. Bas, I. Lisenkov, A. Matyushov, N. X. Sun, and M. R. Page, "Giant nonreciprocity of surface acoustic waves enabled by the magnetoelastic interaction," Sci. Adv. **6**, eabc5648 (2020).

[14]M. Küß, M. Heigl, L. Flacke, A. Hefele, A. Hörner, M. Weiler, M. Albrecht, and A. Wixforth, "Symmetry of the magnetoelastic interaction of Rayleigh and shear horizontal magnetoacoustic waves in nickel thin films on LiTaO3," Phys. Rev. Appl. **15**, 034046 (2021).

[15]M. Küß, M. Heigl, L. Flacke, A. Hörner, M. Weiler, A. Wixforth, and M. Albrecht, "Nonreciprocal magnetoacoustic waves in dipolar-coupled ferromagnetic bilayers," Phys. Rev. Appl. **15**, 034060 (2021).

[16]V. L. Zhang, F. S. Ma, H. H. Pan, C. S. Lin, H. S. Lim, S. C. Ng, M. H. Kuok, S. Jain, and A. O. Adeyeye, "Observation of dual magnonic and phononic bandgaps in bi-component nanostructured crystals," Appl. Phys. Lett. **100**, 163118 (2012).

[17]H. Pan, V. L. Zhang, K. Di, M. H. Kuok, H. S. Lim, S. C. Ng, N. Singh, and A. O. Adeyeye, "Phononic and magnonic dispersions of surface waves on a permalloy/BARC nanostructured array," Nanoscale Res. Lett. **8**, 115 (2013).

[18]P. Graczyk and M. Krawczyk, "Coupled-mode theory for the interaction between acoustic waves and spin waves in magnonic-phononic

crystals: Propagating magnetoelastic waves," Phys. Rev. B **96**, 024407 (2017).

[19]P. Graczyk, M. Zelent, and M. Krawczyk, "Co- and contra-directional vertical coupling between ferromagneticlayers with grating for short-wavelength spin wave generation," New J. Phys. **20**, 053021 (2018).

[20]P. Graczyk, J. Kłos, and M. Krawczyk, "Broadband magnetoelastic coupling in magnonic-phononic crystals for high-frequency nanoscale spin-wave generation," Phys. Rev. B **95**, 104425 (2017).

[21]O. S. Latcham, Y. I. Gusieva, A. V. Shytov, O. Y. Gorobets, and V. V. Kruglyak, "Hybrid magnetoacoustic metamaterials for ultrasound control," Appl. Phys. Lett. **117**, 102402 (2020).

[22]M. F. Limonov, M. V. Rybin, A. N. Poddubny, and Y. S. Kivshar, "Fano resonances in photonics," Nat. Photon. **11**, 543–554 (2017).

[23]R. Fabiha, J. Lundquist, S. Majumder, E. Topsakal, A. Barman, and S. Bandyopadhyay, "Spin wave electromagnetic nano-antenna enabled by tripartite phonon-magnon-photon coupling," Adv. Sci. **9**, 2104644 (2022).

[24]K. Yamanouchi and K. Shibayama, "Propagation and amplification of Rayleigh waves and piezoelectric leaky surface waves in LiNbO3," J. Appl. Phys. **43**, 856–862 (1972).

[25]M. Donahue and D. G. Porter, *OOMMF User's Guide*, Version 1.0, Interagency Report NISTIR 6376 (NIST, Gaithersburg, MD, 1999).

[26]M. Fahim, F. Chowdhury, W. Al Misba, M. M. Rajib, A. J. Edwards, D. Bhattacharya, M. S. Varghese, J. S. Friedman, and J. Atulasimha1, "Focused surface acoustic wave induced nano-oscillator based reservoir computing," Appl. Phys. Lett. **121**, 102402 (2022).

19 December 2023 14:32:54